Original article

Eco-friendly synthesis of functionalized chitosan-based nanoantibiotic system for potential delivery of linezolid as antimicrobial agents

Mahmoud H. Teaima [a],*, Mohamed K. Elasaly [a], Samia A. Omar [b], Mohamed A. El-Nabarawi [a], Kamel R. Shoueir [c],*

[a] Department of Pharmaceutics and Industrial Pharmacy, Faculty of Pharmacy, Cairo University, Cairo, Egypt
[b] Department of Pharmaceutics, Faculty of Pharmacy, Ahram Canadian University, Giza, Egypt
[c] Institute of Nanoscience & Nanotechnology, Kafrelsheikh University, 33516 Kafrelsheikh, Egypt

ABSTRACT

To obtain a healthy human being with beneficial microflora against different pathogenic infections, classical antibiotics with nanosized biomaterials were used to inhibit the growth of bacterium by their potent synergistic effect. Hence, this study planned to load an oxazolidinone antibiotic named linezolid (LD) onto functionalized chitosan (CN) with 3, 5- dinitrosalyslic acid (DA) via microwave synthesis without harsh condition. The exploring synergistic effect of linezolid (LD) with CN/DA controllable nanostructure was compact efflux-mediated methicillin-resistant *Staphylococcus aureus* (MRSA) burden and other selected bactericide Gram-positive (*(S. aureus)*, Gram-negative (*E. coli*), Fungi (*C. albicans*), Yeast (*A. niger*), and *E. faecalis*. The obtained results showed that LD was incorporated into both the internal and external surface of the aggregated CN/DA nanosystem with an average diameter of 150 nm ± 4 hints of the drug loading. Owing to the nature of functionalized CN, the release efficiency attains 98.4% within 100 min. The designed LD@CN/DA exhibited inhibition zone 54 mm, 59 mm, 69 mm, 54 mm, 57 mm, and 24 mm against the tested microbes respectively rather than individual LD. The major target of the current research is achieved by using LD@CN/DA as a nanoantibiotic system that has exceptional consistently active against multi-resistant pathogens, in between MRSA which resist LD. Also, cell viability was performed even after three days of direct cell culture on the surface of the designed nanoantibiotic. The mechanism of microbial inhibition was correlated and rationalized to different charges and the presence of oxygen species against microbial infections. Our findings provide a deep explanation about nanostructured antibiotics design with enhanced potentially pathogen-specific activity.

© 2020 Published by Elsevier B.V. on behalf of King Saud University. This is an open access article under the CC BY-NC-ND license (http://creativecommons.org/licenses/by-nc-nd/4.0/).

1. Introduction

Many diseases caused by Methicillin-Resistant Staphylococcus aureus (MRSA) declare serious wide-world health challenge not less than 2 million morbidities and mortality human rate per year (Hassan et al., 2020). Because of MRSA infections, about more than 80.000 severe infections which increase the rate of death up to 11.000 cases (An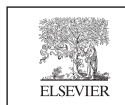dreatos et al., 2018). In Europe, nearly 5.000 deaths cost 700 million$ which MRSA infections no longer stays in hospital and the estimated cost for this regard for each case exceeded 34.000$ (Iqbal et al., 2017). Based on that, acceptable and urgent techniques are currently required to elaborate on new strategies to maximize the benefits of existing conventional antibiotics against bacterial strains (Xie et al., 2018).

There are some of the commonly tested antibiotics against MRSA, such as chloramphenicol, tetracycline, penicillin, aryl thiazoles, and linezolid (LD) behind vancomycin which considered one of the last-resort drugs but the efficacy is not proper. Frequent misuse, a rapid decrease of plasma concentration, and insufficient dose at the infection specific sites are one of the limitations of traditional dosage methods which largely contribute to the resistance between antibiotics and drugs (Gates et al., 1994; Jain et al., 2008). So, a new strategy as a powerful call for penetrating and protecting these antibiotics is being fastened in the literature.

Recently, nanoantibiotic systems based on bio-polymeric structures are being explored to tackle the resistance of antimicrobial problems and find out a true solution for the enhancement of the interaction between antibiotics and bacterial cell walls. Further nanosystems are included micelles (Hasan et al., 2016), nanoemulsion (Jeon et al., 2016), liposomes (Santos et al., 2011), and nano valve (Dwivedi et al., 2018), and biopolymeric sponge nanocarrier (Pawar et al., 2019). Amongst them, polymeric nanocarrier increasing stability and improving the limitations of osmotic shocks related to liposomes and such reported polymers had excellent drug release behavior (Makadia and Siegel, 2011; Salva et al., 2013).

It is well-known that naturally occurred chitosan (CN); the deacetylates product form chitin structure (β– (1–4)-linked D-glucosamine) and is a pioneer amongst polysaccharides in the world for many applications (Shaban et al., 2019; Shoueir, 2020). CN has exceptional characteristics due to its biocompatibility, non-toxicity, the merit of eco-friendly, biodegradability, and significant antibacterial activity. However, assigning to its solubility under acidic condition (pH ~ 4.0) and not appropriate in the common organic solvent, it is seldom to be used in many fields (Atta et al., 2009; Omidi and Kakanejadifard, 2019). These drawbacks may be overcome by suitable chemical modification to enhance functionality, solubility, loading/release, and crystallinity. There are several adopted works introduce different function moieties to CN such as proper Schiff base modification (Ali et al., 2019), crosslinking (Kenawy et al., 2019), carboxymethylation (Wang et al., 2019), and grafting (Sadeghi-Kiakhani et al., 2019) for pharmaceutical applications. However, during the last decades' limited research in the area of delivery of antibiotics using modified CN. Thus, conjugation of CN with other bio-related compounds produces desirable properties in the resulting biofunctionalized polymer with viable applications. 3,5-dinitrosalicylic acid (3,5-DA) amongst different salicylic acid derivatives is used for the detection of reducing sugars owing to its feature as a colorimetric biomedical assay and including different groups –OH, –COOH, and –NO_2 in the structure (Kumar et al., 2016). According to our survey, there is only paper introduces 3,5-DA with CN in the presence of manganese ferrite, and this green combination used for adsorption and photodegradation of pollutants under visible light (Shoueir et al., 2018). The synthetic procedures achieve size reduction and the material synthesis was activated by hydrogen peroxide to compact the adsorption behavior.

The antibiotic oxazolidinones (e.g. Linezolid (LD)) are a new family of an antimicrobial with a unique mechanism of action, superior tissue penetration, and excellent pharmacokinetic index (Stein and Wells, 2010). It is the popular choice of antibiotics for MRSA bacterial treatments besides vancomycin since 2001. Nevertheless, antimicrobial combination therapy may be efficient synergistic to provide broad-spectrum coverage, prevent the emergence of resistant mutants, and obtain a synergy between both antimicrobial agents.

Hereby, the research work was aimed to develop nanoantibiotic biomaterial based on the functionalized chitosan with 3,5-dinitro salicylic acid (CN/DA) loaded with linezolid (LD) as nanoantibiotic system (LD@CN/DA). The designed nanocomposite was examined to evaluate the in-vitro release of LD. The bearing CN/DA encouraging in size reduction to prolong its chemical stability, prevent agglomeration, and increase the charge density at the surface by functionality. A series of physicochemical tools were used to characterize the prepared powerful microwave synthesis of CN/DA. This combination is aggressive against baneful MRSA and other selected different test microbes namely: *Staphylococcus Aureus* ATCC 6538 (G + ve), *Enterococcus faecalis* ATCC 29212 (G + ve), *Escherichia Coli* ATCC 25922 (G-ve), *Candida Albicans* ATCC 10231 (yeast) and *Aspergillus Niger* NRRL A 326 (fungus). As such trend

is mandatory to employ nano-formulation based on the green principles to overcome antimicrobial drug resistance owing to biocompatibility and cytotoxicity which also tested.

2. Materials and methods

2.1. Microwave fabrication of CN/DA nanostructure

About 1 g of CN (75–85% deacetylated, 50,000–190,000 Da, Sigma-Aldrich) was dissolved in 50 mL of distilled water containing 0.1 mL of glacial acetic acid (analytical grade) with moderate stirring. Then after, 1.51 g of DA (Sigma-Aldrich) was mixed with consecutive 9.11 mL DMF (analytical grade) and 7.75 mL formaldehyde (analytical grade, 37–40%). The later content was added to the CN solution for 30 min in a 250 mL round flask to produce a yellow slurry solution. All the reaction solution was transferred to microwave reactor with PTFE tubes (WX-4000) with the following parameters: 40% stirring rate, 1000 W, temperature 75 °C, equilibrium time 40 min, and 0.8 Par. After the machine stopped, the observed precipitated powder was washed several times with water and absolute ethanol to remove solvents and any unreacted chemicals. Finally, the scarlet yellowish product was dried for 24 h under vacuum at 55 °C. For drug loading, 3 mg/mL of LD was dissolved batch-wise in ethanol which powdered CN/LD was added drop-wise under vigorous stirring for 12 h at 37 °C to prevent solvent interaction. The ratio of LD to CN/DA was equilibrated at 1:2 (W/W) (Abdelbar et al., 2020). Then, the suspension was centrifuged at 10.000 rpm for 45 min. The supernatant was removed and pure form of LD@CN/DA was collected and washed again twice with ethanol, dried, and kept before use.

2.2. Physicochemical characterization

FTIR spectra (Model no. 4000, JASCO, Japan) spectrophotometer adjusted in range 4000–500 cm^{-1} to prove the chemical structure after the samples were mixed with KBr pellets to obtain solid disk before measure. The ^{13}C NMR spectrum (BRUKER, USA) was measured and recorded at 100 MHz. High-Resolution Transmission electron microscope (HR-TEM, JEOL 2100) used to affirm the CN/DA nanostructure operating at 200 keV. The CN/DA was stained before use, and then 1 mg of samples were dispersed and sonicated in ethanol for 5 min before fixed on the copper grids, dried, and examined using TEM. Malvern Instruments Ltd, UK, dynamic light scattering (DLS, Zen 1600 Malvern USA, Ltd) to measure the hydrodynamic size of green CN/DA. Scanning electron microscope (SEM, QUANTA FEG250) was used to identify the surface morphology of samples after complete drying then after, sputtered with gold before observation. SEM unit was a pendant with an external Energy Dispersive X-ray (EDX). The typical XRD patterns for phase structure were acquired on a Philips X Pert diffractometer. Alpha 300-A Atomic force microscopy (AFM) WITec, Japan, to study the surface roughness of CN/DA and synergistic LD@CN/DA. The thermal degradation as a function of weight loss (mg) was measured by TGA analysis (AT Instrument Q500) at 20 kV and the temperature range from 10 to 800 °C. Multipurpose UV–Vis double beam spectrophotometer (Shimadzu UV-2600) was used to measure the concentration of LD.

2.3. Determination of entrapment efficiency of LD loaded CN/DA nanosystem

Firstly, it is observed that the encapsulated drug-loaded CN/DA -based nanoantibiotic system was completely soluble in phosphate buffer solution prepared at two different pH; pH 5.0 and 7.0 affirming that there is no effect for the acid or alkaline medium on the

degradation of efficiency of the drug. Consequently, in the present study, the solubility was enhanced during the presence of charged nanoparticles CN/DA which is a mild condition of preparation. The drug entrapment capacity (E%) was detected by an ultrafiltration method (Wang et al., 2017). About 5 mL of formulated LD@CN/DA was loaded into Millipore UFC910024 Amicon Ultra Centrifugal Filter, 15 mL Capacity, 100 kDa pore size and centrifuged at 9000 rpm at room temperature for 30 min. The amount of unattached LD in the supernatant was detected spectrophotometrically at λ max 250 nm. The regression equation of Y = 0.05X + 0.0029, with correlation coefficient R^2 = 0.998, was used to detect the unbound LD concentration values and compared with a cited calibration curve of LD in the water at different concentrations ranging from 10 to 40 µg/mL. The designed experiment was repeated thrice at least, and the following formula was used to calculate the encapsulation efficiency of LD loaded CN/DA:

$$E(\%) = \frac{D_1 - D_0}{D_1} x 100 \qquad (1)$$

where E%, D_1, and D_0 expressed the encapsulation efficiency percentage, the initial amount of LD, and the unbounded LD respectively.

2.4. In vitro LD release study from the nanocomposite (LD@CN/DA)

Release behavior was examined based on two main various 50 mL phosphate buffers: PBS 5.0 and 7.4 to mimic different pHs environment (Azmy et al., 2019). The resultant LD@CN/DA was suspended in 5 mL of mentioned PBS and then dialyzed using a dialysis bag with a porosity of 8.000 to 14.400 Da against 50 mL PBS at 37 °C for 48 h in shaking incubator at 150 rpm under dark condition. The released medium was withdrawn at fixed time intervals and replenished with fresh medium. The absorbance was calculated at exactly 250 nm at time intervals by using the calibration curve of LD as reference. The release fraction from LD@CN/DA was calculated according to the following formula:

$$LD cumulative release(\%) = \left(\frac{A_t}{A_v}\right) X 100 \qquad (2)$$

where A_t is the amount of released LD from CN/DA nanostructure at predetermined time t, and A_v the amount of LD previously-loaded inside LD@CN/DA formulation.

2.5. Antimicrobial activity assays in vitro study

LD, CN/DA, and LD@CN/DA in a concentration 2 mg.mL^{-1} were prepared and tested separately for their antimicrobial activities against the provided test microbes. The test microbes used are *MRSA*, *E. Fecalis*, *S. aureus* ATCC 6538 (G + ve), *E. Coli* ATCC 25922 (G−ve), *C. albicans* ATCC 10231 (yeast) in addition to *A. Niger* NRRL A 326 (fungus). Nutrient agar plates were used in the case of bacteria and yeast test microbes. Each plate was seeded uniformly with 0.1 mL of 10^7–10^8 cells/ml from bacterial and yeast test microbes. Whereas, Potato Dextrose agar plates were used to evaluate the antifungal activities. Then a cup (1 cm diameter) was made in media by gel cutter (Cork borer) in a sterile condition. Then one drop of melted agar was poured into the hole and allowed to solidify to make a base layer. After that specific amount of tested sample (100 µL) was poured into the cup. Then plates were kept at low temperature (4 °C) for 2–4 h to allow maximum diffusion. The plates were then incubated at 37 °C for 24 h for bacteria and 30 °C for 48 h in an upright position to allow maximum growth of the organisms. The antimicrobial activity was determined by detecting the diameter of the zone of inhibition expressed in millimeter (mm). The experiment was carried out more than once and the mean of reading was recorded.

2.6. In vitro cell culture evaluation

The cytocompatibility of the designed CN/DA nanostructured was investigated using human cell line PC3 (Prostate carcinoma). Before seeding, CN/DA samples with serial concentrations (200–3.125 µg/mL) were soaked in absolute ethanol for 15 min and subjected to UV light for one hour before sterilization, then soaked in PBS thrice for further complete purification. Briefly, PC3 was seeded into 48-plate and cultured in Dulbecco's modified Eagle's medium (DMEM, Gibpco) at 37 °C and the presence of a humid atmosphere involving 5% CO_2 for one day. Afterward, the selected cell was seeded with a specific density of $5X10^3$ cells/cm^2 onto the sterilized nanoparticles. After 5 days in an incubator, the media was removed and MTT (3-(4,5-dimethylthiazol-2-yl)-2,5-diphenyl tetrazolium bromide) was injected into each well. 150 µL of Kit-8, CCK-8 solution was used to count the cell viability on tested nanoparticle concentrations for 1, 3, and 5 days. Cell viability is defined as the percentage of viable cells compared to the total cell number and expressed as follows (Song et al., 2020).

$$Viability(\%) = \frac{Mean optical density of test samples}{Mean optical density of the control} \times 100 (n = 5) \qquad (3)$$

2.7. Statistical analysis

The provided data were achieved in triplicate and expressed as mean ± the standard deviation (SD, n = 3). The significant difference analysis was determined using analysis of variance (ANOVA) via Minitab software (version 19.1.1.0). The level of P < 0.05 is the statistical significant bar.

3. Results and discussion

3.1. Structural, morphological, and topography analysis

3.1.1. UV–Vis detection
Fig. 1 shows the electronic spectrum of the CN and CN/DA nanoparticles. CN is too far-UV chromophoric moieties, glucosamine, and N-acetyl-glucosamine; therefore, its extinction coefficients for wavelengths less than 250 nm are due to its
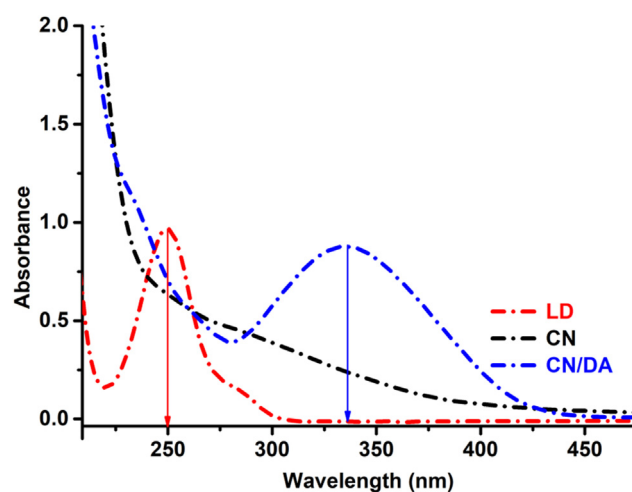

Fig. 1. Absorbance spectrum of CN and CN/DA.

transparency. The reaction between CN and DA showed a wide band at position 335 nm owing to n → π* transition in –NH groups. In addition, the presence of aromatic nucleus indicates π → π* allowed transition of NO_2, C = N chromophoric groups that are conjugated with polysaccharide structure (Abdelbar et al., 2018; Demetgül and Beyazit, 2018). Also, the UV scan of LD was detected and showed the absorption maxima at exactly 250 nm.

3.1.2. ^{13}C NMR chemical shifts

The ^{13}C NMR spectrum of the prepared CN/DA is shown in Fig. 2. The chemical shifts of CN (C_1-C_6) are matching with the bases of published elsewhere (Wang et al., 2016). The intense peak at 49.21 ppm (C_7) ascribed to the methylenic carbon bridge of Ar-NH-CH_2 moiety. For C8, it appeared at 129.2, and the peak at 169.23 ppm (C_9) related to the –C = O of Aromatic-COOH function (Khan et al., 2013). Other detected peaks from C_{10} to C_{13} appeared at 164.51, 129.11, 123.45, and 138.2 ppm in the CN/DA structure are attributed to 3,5-DA.

3.1.3. FT-IR spectral analysis

The FTIR spectra for CN and CN/DA were performed to outline the change in their chemical structure and the produced graphs are displayed in Fig. 3. For CN, the demonstrated peak at 3473 cm^{-1} is consigned for the stretching vibration mode of both N-H and O-H groups. Meanwhile, the bands observed at 2872 cm^{-1}, 2917 cm^{-1}, 1590 cm^{-1}, and 1378 cm^{-1} are assigned to –CH chain stretching mode, amide I, amide II (amine ν (NH_2) tensions), and CH_3 symmetrical angular deformation, respectively (Atta et al., 2009, 2015; Shoueir et al., 2017). The peak that ascribed at 1089 cm^{-1} peak is owing to the absorbance of β-1–4 glycosides linkage (Qi et al., 2004). Moving to the FTIR of CN/DA, it is observed that there are additional peaks are observed. For example, the broadband with shift location from 3455 cm^{-1} to 3394 cm^{-1} is attributed to the existence of OH groups connected C = O of DA aromatic ring. Furthermore, there is a newly formed peak at 3097 cm^{-1} which could be related to the stretching modes of –CH in the aromatic ring (Sebastian et al., 2015). The newly detected band at 2359 cm^{-1} is appointed for –CH_2 linkage between CN-CH_2-3,5-DA (Riswan Ahamed et al., 2015). Factual augmentation of –CH bond turns out to be significant since the distortion asymmetric –CH_2 band at 1499 cm^{-1} and symmetric –CH_2 at 1347 cm^{-1}. Other intense, the observed medium and weak peaks between 703 and 1279 cm^{-1} are correlated to substituted 3,5-DA (Pretsch et al., 2013). Based on these witnessed peaks, the spectrum discloses that DA functionalized CN was effectively incorporated and the suggested mechanism is obtainable in Scheme 1. From the previous
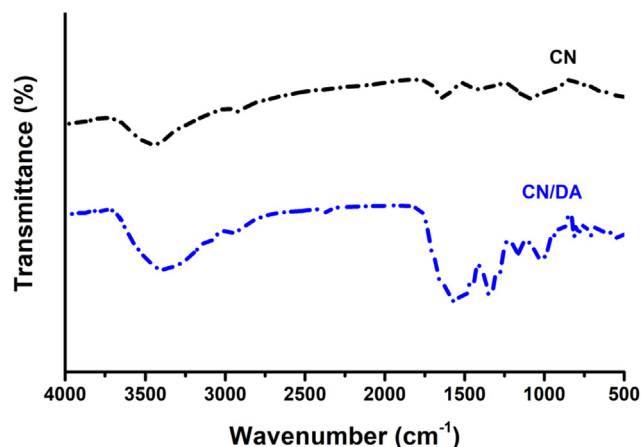

Fig. 3. FT-IR spectra of CN and CN/DA.

^{13}C NMR and FTIR spectral data, the anticipated structure of CN/DA has been confirmed.

3.1.4. TEM and SEM analysis

To explain the particle shape of the formed nanoparticulate system, the TEM technique has been conducted. Thus, Fig. 4 displays the TEM image of an eco-friendly prepared CN/DA. As shown in Fig. 4a the produced CN/DA two possible structures (violet square) with irregular shapes. In addition, it is depicted that most DA is attached to the surface of CN particles, and some of them being incorporated into the interconnected CN network. The particles have an average diameter size of 50 ± 2 nm, which in accordance with the obtained data from DLS. For clarification of the morphological structure, SEM was performed at high magnification and then implemented in Fig. 4b which demonstrates the surface of the scanned nanoparticles exhibits agglomerated spherical particles, porous, and roughness structure with clear edges. Because of the compatibility among the reactants, both spherical particles and the presence of pores structures support efficiency drug loading. Besides, the CN chain is effectively linked to DA as a biopolymer (Fan et al., 2017). EDX spectrum has also been shown to include C, N, and O in the sample (Fig. 4c) as well as the elemental mapping (Fig. 4d) which indicates that of the nanoparticulate system revealed that N and O atoms are major constituents and evenly distributed around the backbone. Fig. 4e displays the highly crystalline material of pure LD morphology with sheets like structure and their length is more than 30 μm. It is seen that LD is effectively incorporated into the aggregated modified CN (Fig. 4f) (El-Shabasy et al., 2019; Tammaro et al., 2015) which determine very different kinetics of release. Moreover, LD easily crystallizes in different polymorphs phases or an amorphous structure which beneficial in its release rate.

3.1.5. XRD crystallography

Typical XRD patterns are shown in Fig. 5; there is no change in the spinal structure after adding of DA to CN, assuming that this modification had no obvious effect on the crystal phase of CN. The manifest diffraction peaks at 2θ = 37.47°, 44.0°, 64.34°, and 77.54° still as it is before modification except, 2θ = 19.7° this corresponding peak was deeply broadened owing to the insertion and compatibility of DA. Therefore, the peak intensity was reduced owing to the steric hindrance effect (Yusof et al., 2019), further confirming the introduction of DA into the CN network.
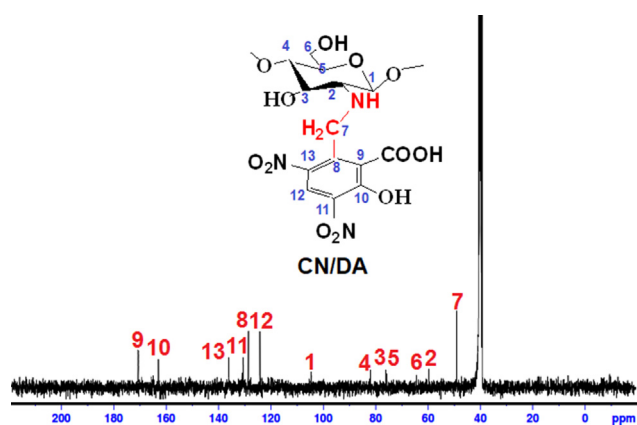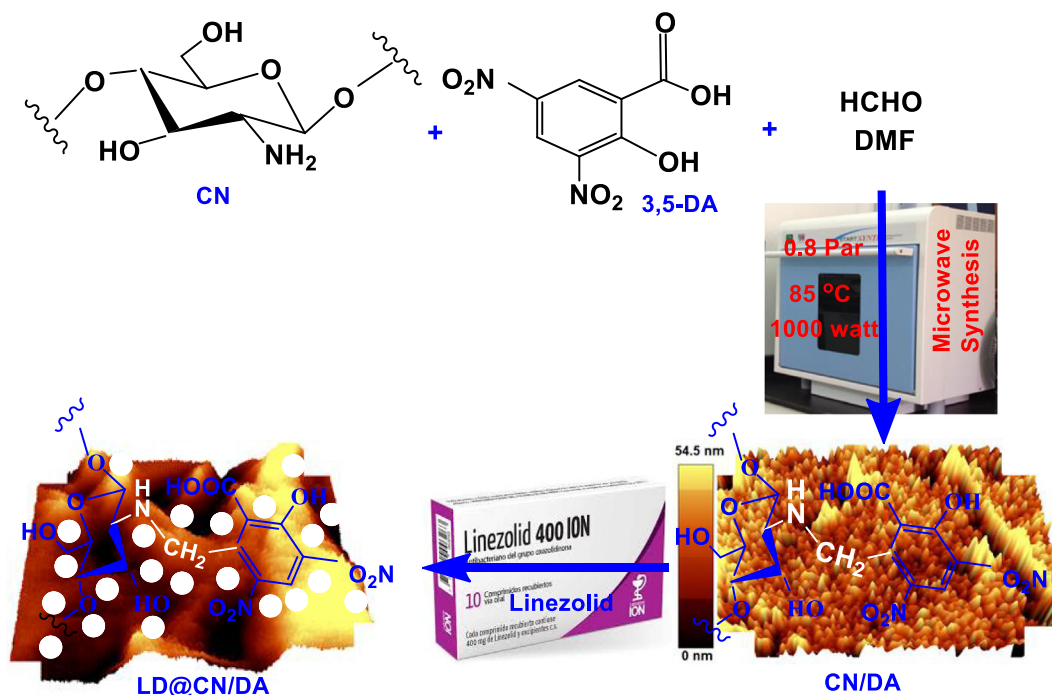

Fig. 2. Structure elucidation of CN/DA by ^{13}C NMR spectrum.

Scheme 1. Postulated sequence for the synthesis of CN/DA and the possible interaction with LD.

3.1.6. AFM topography module

Fig. 6 shows the three-dimensional topography AFM image. The surface of CN/DA is very small nodes like grains that are arbitrarily dispersed along the surface. The calculation of average surface roughness was 54.5 nm, which consistent with size measured from HR-TEM analysis suggesting that the surface is rough. As stated in literature any increment in surface roughness is amenable for delivering adsorption saturation (Kumar et al., 2014; Shoueir et al., 2020). Addition of LD exhibit hairy with uniform level grooves which increased the surface area of CN/DA towards adsorption of selected antibiotics.

3.1.7. Thermal stability

Fig. 7 displays TGA and DTA curves for synthesized CN/DA collected up to a higher 800 °C under the N$_2$ atmosphere. The first distinct decomposition temperature occurs at 199.68 °C (16.64%), which is higher stable than that of previously reported pristine CN (Murali et al., 2019). The methylene linkages are responsible for such stability, and complete decomposition from 600 °C has been attributed to the deterioration of the aromatic DA ring and the loss of the polysaccharide ring.

3.2. In vitro release profile of bare LD from the CN/DA nanostructured

The entrapment efficiency of LD drug-loaded the green synthesized CN/DA is a principle to determine the capability of the carrier for drug loading. The optimal entrapment potency of LD loaded into CN/DA nanostructured was found to be 95.71% at low pH. As shown in Fig. 8 the two curves of the released profile under two different PBS 5.0 and 7.4 buffers via the direct dispersion technique. Regardless of the nature of both CN/DA and LD the release profile was divided into two steps. In the first stage, the LD has burst release equal to 93.13 (5.0) rather than 61.96% (7.4) in 60 min. The initial burst exists in a lot of controlled systems as the mechanism dependent on pore diffusion, surface desorption, or repulsive force between opposite charges (Pawar et al., 2019). Thereafter, the release followed by a controlled release of LD from the

CN/DA nanostructure where the selected LD was released continuously for up to 100 min to attain maximal 98.43% compared with 85.17% in the two PBS. This returned to the biocompatibility between nanoparticles and the drug near the surface as examined in the SEM section and also related to the more crystalline phase of LD molecules tend to encapsulate inside the nanoparticles. Indicating that this type of modification might be valid in providing drug release to some extent (Li et al., 2018a). On the other side, pH is a crucial effect on the drug release pattern due to here the swelling parameter of the as-synthesized modified CN (Atta et al., 2009; Esmaeili and Ghobadianpour, 2016). Furthermore, at low pH, the amino and carboxylic acid groups in CN/DA were protonated and extend repulsive interaction between neighboring positive charges, consequently swelling ability increased facilitates LD elution. In alkaline medium, the network shrank and thus, hinders the spreading of LD.

3.3. Determination of antimicrobial inhibition zone

The antimicrobial efficacy of LD, CN/DA, and LD@CN/DA as nanoantibiotic were examined using many different species of microbes such as *S. aureus*, *E. faecalis*, *E. coli*, *C. Albicans*, and *A. niger* as well. The evaluation was calculated via determining the inhibition zone diameter after submitting the designated compounds for analysis and the obtained data are outlined in Table 1 and Fig. 9. It has been depicted that the diameter (mm) of the killed microbes due to the antimicrobial effect of LD was 44 mm, 65 mm, 22 mm, 52 mm, and 25 mm for all tested microbes respectively. It has been observed that the efficacy of LD for killing or prevent the diffusion of microbes follows the order; *E. faecalis* > *C. Albicans* > *S. aureus* > *A. niger* > *E.coli* which means that *E. faecalis* more sensitive than the other tested microbes towards the effect of LD. It has been also proved that the polymer; CN/DA provided a little effect as an antimicrobial against the examined MRSA and *E. faecalis* microbes only. While the combination of LD@CN/DA registered superior antimicrobial properties towards all tested microbes. The inhibition zone value was 54 mm, 69 mm and
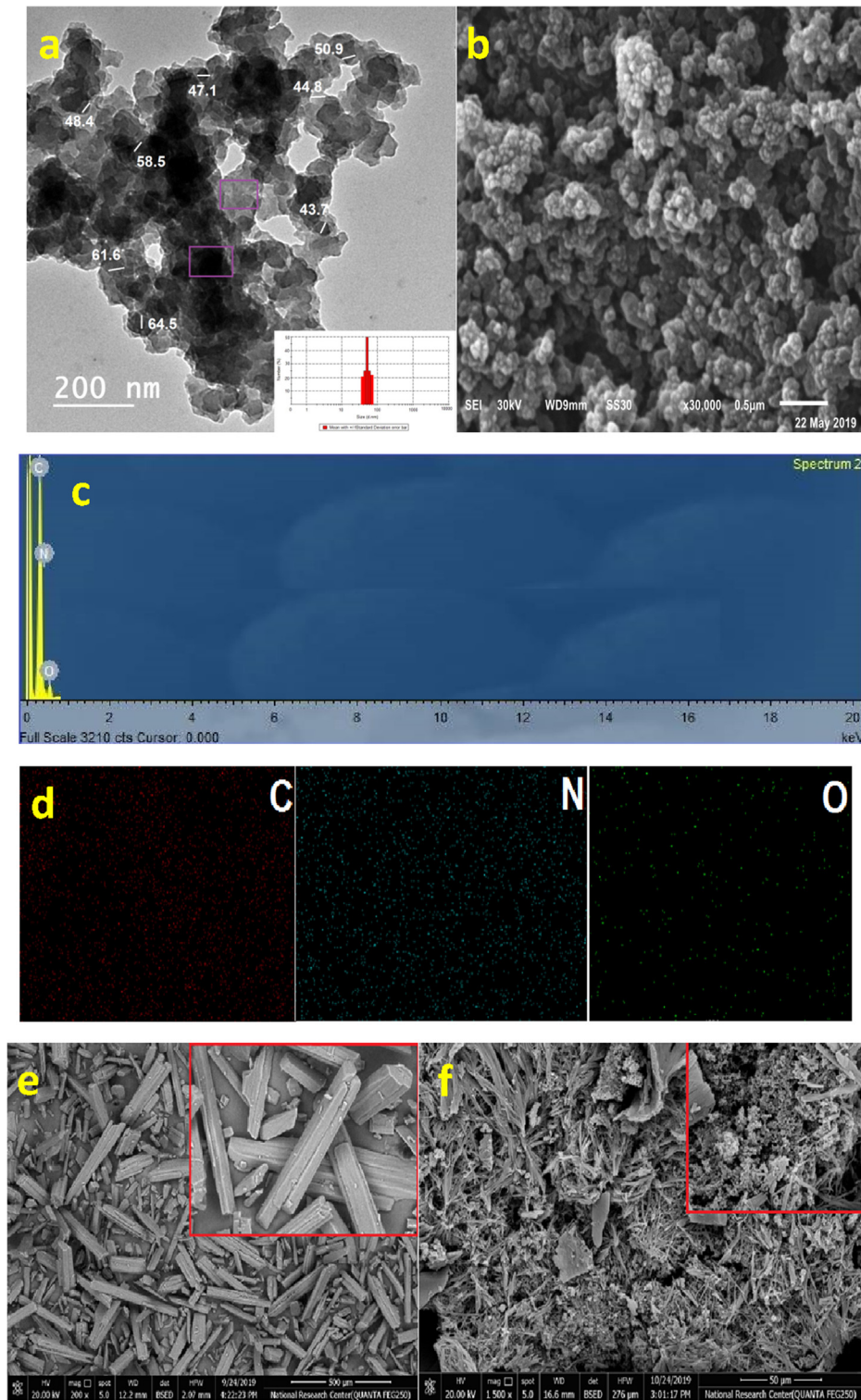
Fig. 4. (a) HR-TEM image, (b) FE-SEM morphology, (c) EDX analysis, (d) mapping area of CN/DA, (e) surface morphology of pure LD, and (f) relative LD morphology after interaction with CN/DA.

54 mm, 57 mm, and 24 mm for *S. aureus*, *E. faecalis*, *E. coli*, *C. Albi-cans*, and *A. niger* respectively which exhibit higher value more than that of LD. Additionally, the antimicrobial investigation was extended to be evaluated against MRSA. It has been proven that LD exhibit higher antimicrobial properties equal to 55 mm against MRSA. The moderated antimicrobial properties of CN/DA have

been detected against the nominated microbes; MRSA (33 mm). Meanwhile, the antimicrobial has been greatly enhanced during the utilization of nanoantibiotic against MRSA (59 mm). The greater effect for the latter nanocomposite could be attributed to the high surface area which enhances the easy penetration of the nanoparticulate system inside the walls of the tested microbes.
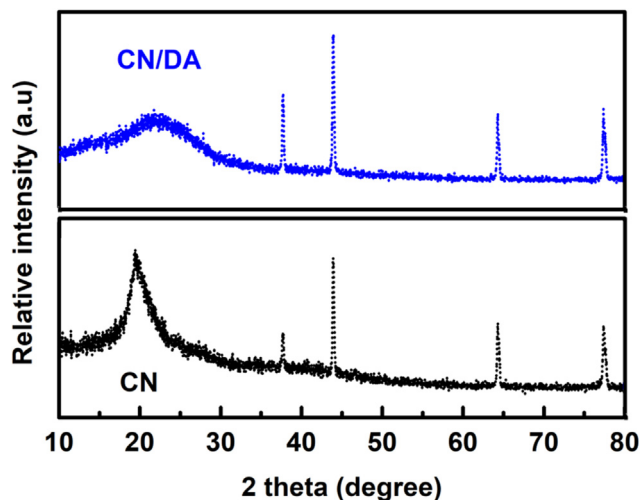
Fig. 5. XRD crystallography of pure CN and CN/DA.

Fig. 7. TGA-DTA thermogram of CN/DA.

Based on the aforementioned results, it can be concluded that the antimicrobial properties of LD@CN/DA are greater than that of LD and CN/DA compounds.

3.4. Cytocompatibility of the CN/DA matrix

Since the prepared CN/DA was identified as biomaterials when dealing with the body, so it is expected that there is no toxicity. According to CCK-8 counting cell viability assay, CN/DA extends higher relative cell viability especially at a higher concentration which tended to positive effect to harvests 97.3% cell adhesion with PC3 after one day, providing good biocompatibility. So, introducing this type of antibacterial bio-nano functionality is important not only in the particle formation but also in the enhancement of cell interactions and protein adsorption (Huang et al., 2019; Salama et al., 2018). Moreover, the cytotoxicity is directly proportional with the time to kill 89.4, 92.8, and 97.3% from the targeted cancer cells after 24, 48, and 72 h respectively (Fig. 10). Considering the results, the nanostructured CN/DA exerted higher cytocompatibility and non-toxicity with relative cell viabilities more than 85% which able to form an effective nanoantibiotic system and classified as cytocompatible (Li et al., 2018b).

3.5. A suggested mechanism for the interaction between CN/DA and LD@CN/DA with the bacterial cell membrane

It is well known that LD is a synthetic antibiotic belongs to a new class of antimicrobials called the oxazolidinones. The initia-
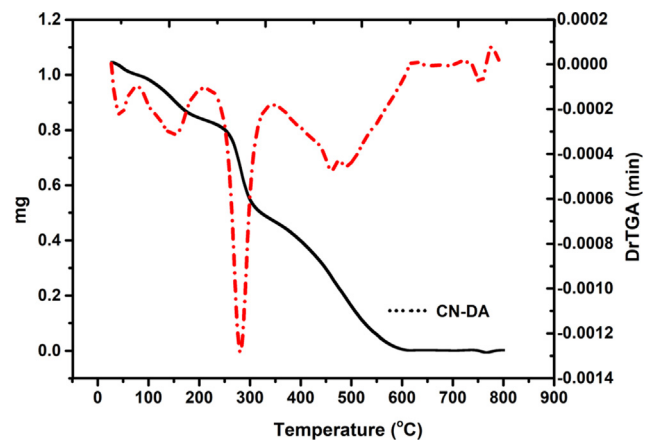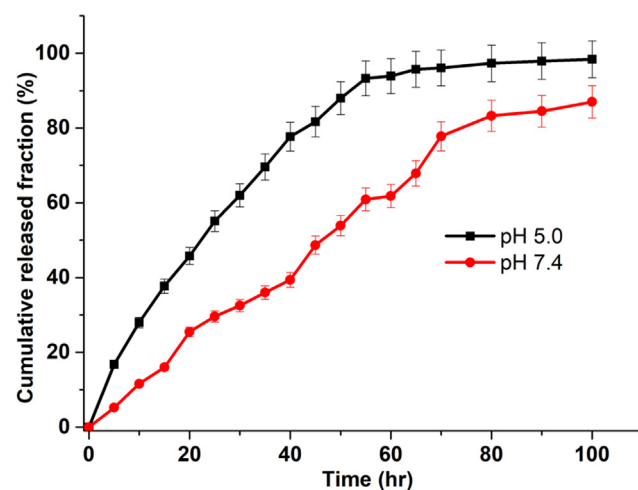

Fig. 8. *In vitro* drug release profile of bare LD at pH 5.0 and pH 7.4 (n = 3).

tion process for the growth of microbes was carried out by disrupts the process due to the effect of the LD molecule. As identified, this initiation process has been prevented for the protein biosynthesis via binding at the 50S ribosomal subunit consequently inhibit the initiation phase of translation (Shinabarger, 1999). In some cases, the bacterial resistance of LD may be attributed to the high potency effect of LD against selected bacterial strain when combined with prepared nanoparticles CN/DA (Shoueir, 2020 #146). In our work, LD@CN/DA nanostructured composite was formed by chemical reaction of CN with DA. The chemical reaction has
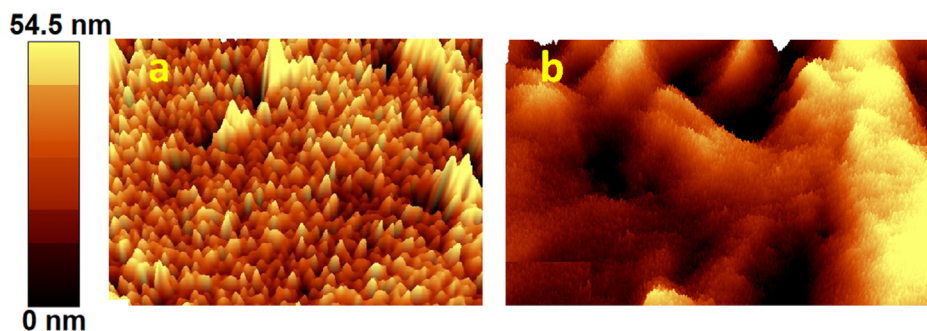

Fig. 6. AFM topography of green (a) CN/DA and (b) LD interacted with CN/DA.

Table 1
The antimicrobial activities of LD, CN/DA and LD@CN/DA nanosystems against different test microbes.

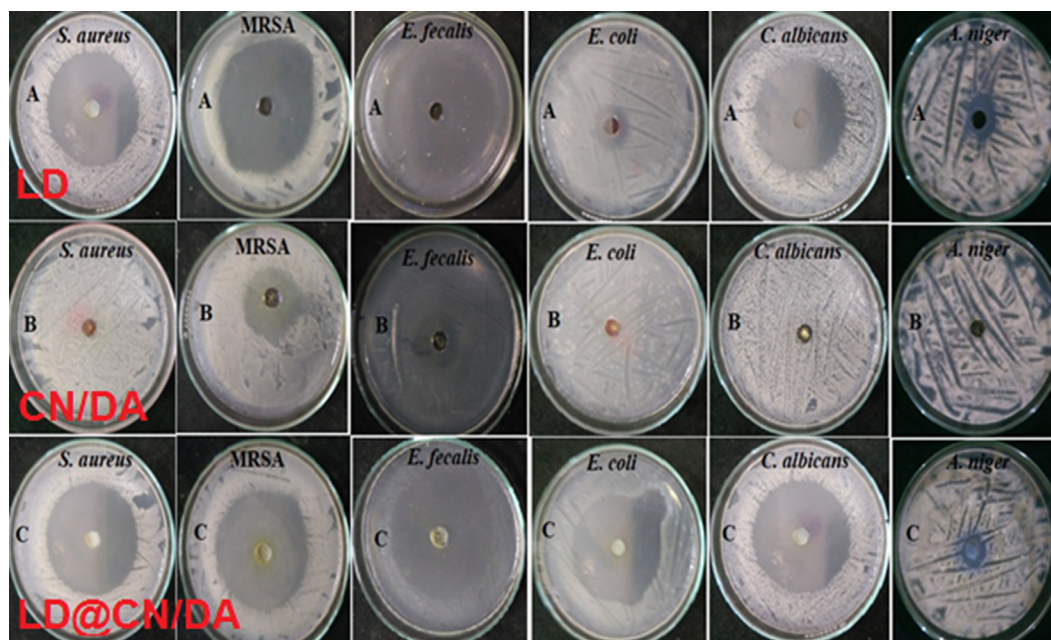| Clear zone (φmm)						Sample name	Serial no
Aspergillus niger	Candida albicans	Escherichia coli	Enterococcus faecalis	MRSA	Staphylococcus aureus		
25	52	22	65	55	44	LD	A
0	0	0	26	33	0	CN/DA	B
24	57	54	69	59	54	LD@CN/DA	C

Fig. 9. The exact inhibition zone of (a) LD, (b) CN/DA, and (c) LD@CN/DA nanoantibiotic towards MRSA and other microbes.
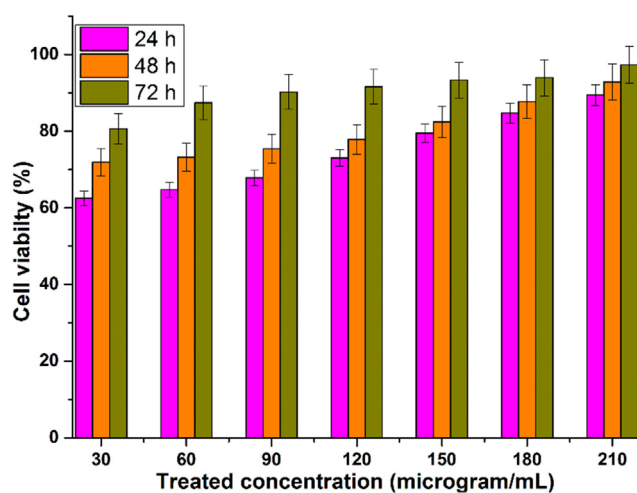

Fig. 10. Cytotoxicity assessment at higher concentration quantification post 24, 48, and 72 h treatment ($p < 0.05$).

occurred via methylation reaction and ultimately, LD has been loaded onto the surface charged CN/DA. Moreover, the antimicrobial properties may be enhanced due to the attack of positively charged CN to the negative charge bacterial cell. Additionally, the utilization for using DA is to stabilize the formed CN and prevent its aggregation and thus, maintain its size in a very small size with good distribution and easily bring into being the death of microbial cell death (Prokhorov et al., 2019). Another postulate can be concluded from the generation of oxygen species and other free radicals due to the interaction of LD@CN/DA with microorganisms. These active species destroy and stop the replication of microbes' intracellular components via interaction with the main components of microbes such as lipids, phosphorous DNA, and sulfur proteins. Likewise, the topographical changes in the outer membrane should direct to a slight modification in the configuration of the cell structure. Fig. 11 produces a topographical evaluation of aggravation between nanoantibiotic with MRSA and selected C. Albicans from other microbes. In Fig. 11a (dark field), the optical microscope of control polymorphic LD in highly crystalline order, with brought into contact with modified chitosan it has entrapped onto an internal and external surface (Fig. 11b light field) as discussed in SEM section. It has been noted from Fig. 11c that LD@CN/DA exhibit small size with stable multiple layer structure. Also, it is observed that the surface of LD@CN/DA exhibit two different nanonetwork layers due to the adsorption of LD onto the surface of CN/DA causes marginally increase in the viscosity of the solution, which in turn, leading to enlargement the produced particles with attacking bacterial cells (Pinheiro et al., 2015). The change in the morphological shape in the cell surface of MRSA became irregular and structural invagination alterations compared to Fig. 11c inset. Furthermore, MRSA cell membrane damage induced by nanosystems as it provokes the burst of intracellular components such as phosphates, potassium (small ions), and large molecules including DNA, RNA, and proteins. After confirming that the nanoantibiotic system had elegant activity on the MRSA, also the effect of the designed
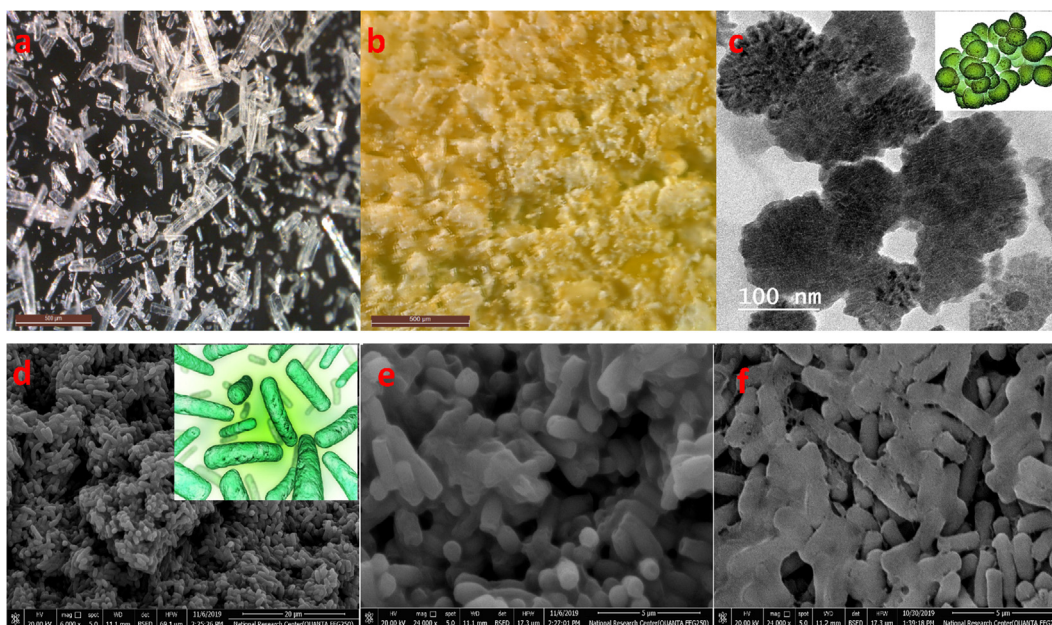
Fig. 11. (a) Optical microscope of LD under dark field, (b) LD contact with CN/DA, (c) TEM of MRSA cell wall distortion when exposed to nanoantibiotic, (d) *C. albicans* without treatment, (e) initial contact with nanoantibiotic, and (f) complete disruption of *C. albicans* after 3-hours.

nanosystems on the membrane of *C. albicans* was studied. In Fig. 11 (d-f) and after incubation of bacteria there was noticed that a great loss and disruption of bacteria membrane after three hours causing permanent death. Via obtaining the LD@CN/DA with small size and good distribution, it is expected that such the prepared nanosystems (LD@CN/DA) provides us a good prediction and deep thinking for the development of newer antibacterial agents that can be used in pharmaceutical industries.

4. Conclusion

A new design of nanoantibiotic is urgently warranted to combat against bacteria such as fatal MRSA and other microbes. The green approach of prepared CN/DA was discussed and characterized to affirm the nature of surface and availability to payload LD antibiotics. The constructed CN/DA exhibited irregular shapes with two possible structures and hairy with uniform grooves structure was obtained during interaction with LD antibiotic. The designed CD/LD scaffold release 98.43% LD under low pH within 100 min owing to the biocompatibility between nanoparticles and the drug near the surface. The inhibition diameter was 54, 54, and 24 mm, for *S. aureus*, *E. coli*, and *C. Albicans* which also tested and exhibit higher value compared to separate LD. Also, our results reveal that LD@CN/DA induces severe damage on the MRSA bacterial cell membrane led to the loss of membrane integrity and their intracellular components followed by cell death. Besides, the cell viability was eradicated 97.3% from the PC3 carcinoma cell line after three days which registered as cytocompatible materials. We believe that the constructed synergistic LD with CN/DA has promising candidates in the field of industrial pharmacy.

Declarations of Competing Interest

The authors declare that there is no conflict of interest.

References

Abdelbar, M.F., El-Sheshtawy, H.S., Shoueir, K.R., El-Mehasseb, I., Ebeid, E.-Z.M., El-Kemary, M., 2018. Halogen bond triggered aggregation induced emission in an iodinated cyanine dye for ultra sensitive detection of Ag nanoparticles in tap water and agricultural wastewater. RSC Adv. 8, 24617–24626.

Abdelbar, M.F., Shams, R.S., Morsy, O.M., Hady, M.A., Shoueir, K., Abdelmonem, R., 2020. Highly ordered functionalized mesoporous silicate nanoparticles reinforced poly (lactic acid) gatekeeper surface for infection treatment. Int. J. Biol. Macromol. 156, 858–868.

Ali, S.S., Kenawy, E.-R., Sonbol, F.I., Sun, J., Al-Etewy, M., Ali, A., Huizi, L., El-Zawawy, N.A., 2019. Pharmaceutical potential of a novel chitosan derivative Schiff base with special reference to antibacterial, anti-biofilm, antioxidant, anti-inflammatory, hemocompatibility and cytotoxic activities. Pharm. Res. 36, 5.

Andreatos, N., Shehadeh, F., Pliakos, E.E., Mylonakis, E., 2018. The impact of antibiotic prescription rates on the incidence of MRSA bloodstream infections: A county-level, US-wide analysis. Int. J. Antimicrob. Agents 52, 195–200.

Atta, A.M., Abdel-Bary, E., Rezk, K., Abdel-Azim, A., 2009. Fast responsive poly (acrylic acid-co-N-isopropyl acrylamide) hydrogels based on new crosslinker. J. Appl. Polym. Sci. 112, 114–122.

Atta, A.M., El-Mahdy, G.A., Al-Lohedan, H.A., Shoueir, K.R., 2015. Electrochemical behavior of smart N-isopropyl acrylamide copolymer nanogel on steel for corrosion protection in acidic solution. Int. J. Electrochem. Sci 10, 870–882.

Azmy, E.A., Hashem, H.E., Mohamed, E.A., Negm, N.A., 2019. Synthesis, characterization, swelling and antimicrobial efficacies of chemically modified chitosan biopolymer. J. Mol. Liq. 284, 748–754.

Demetgül, C., Beyazit, N., 2018. Synthesis, characterization and antioxidant activity of chitosan-chromone derivatives. Carbohydr. Polym. 181, 812–817.

Dwivedi, A., Mazumder, A., Nasongkla, N., 2018. Layer-by-layer nanocoating of antibacterial niosome on orthopedic implant. Int. J. Pharm. 547, 235–243.

El-Shabasy, R., Yosri, N., El-Seedi, H., Shoueir, K., El-Kemary, M., 2019. A green synthetic approach using chili plant supported Ag/Ag2O@ P25 heterostructure with enhanced photocatalytic properties under solar irradiation. Optik 192, 162943.

Esmaeili, A., Ghobadianpour, S., 2016. Vancomycin loaded superparamagnetic MnFe2O4 nanoparticles coated with PEGylated chitosan to enhance antibacterial activity. Int. J. Pharm. 501, 326–330.

Fan, C., Li, K., Li, J., Ying, D., Wang, Y., Jia, J., 2017. Comparative and competitive adsorption of Pb (II) and Cu (II) using tetraethylenepentamine modified chitosan/CoFe2O4 particles. J. Hazard. Mater. 326, 211–220.

Gates, K.A., Grad, H., Birek, P., Lee, P.I., 1994. A new bioerodible polymer insert for the controlled release of metronidazole. Pharm. Res. 11, 1605–1609.

Hasan, M., Messaoud, G.B., Michaux, F., Tamayol, A., Kahn, C., Belhaj, N., Linder, M., Arab-Tehrany, E., 2016. Chitosan-coated liposomes encapsulating curcumin: Study of lipid–polysaccharide interactions and nanovesicle behavior. RSC Adv. 6, 45290–45304.

Hassan, D., Omolo, C.A., Fasiku, V.O., Mocktar, C., Govender, T., 2020. Novel chitosan-based pH-responsive lipid-polymer hybrid nanovesicles (OLA-LPHVs) for delivery of vancomycin against methicillin-resistant Staphylococcus aureus infections. Int. J. Biol. Macromol. 147, 385–398.

Huang, L., Zhu, Z., Wu, D., Gan, W., Zhu, S., Li, W., Tian, J., Li, L., Zhou, C., Lu, L., 2019. Antibacterial poly (ethylene glycol) diacrylate/chitosan hydrogels enhance mechanical adhesiveness and promote skin regeneration. Carbohydr. Polym. 225, 115110.

Iqbal, H., Ponniah, N., Long, S., Rath, N., Kent, M., 2017. Review of MRSA screening and antibiotics prophylaxis in orthopaedic trauma patients; the risk of surgical

site infection with inadequate antibiotic prophylaxis in patients colonized with MRSA. Injury 48, 1382–1387.

Jain, N., Jain, G.K., Javed, S., Iqbal, Z., Talegaonkar, S., Ahmad, F.J., Khar, R.K., 2008. Recent approaches for the treatment of periodontitis. Drug Discovery Today 13, 932–943.

Jeon, Y.O., Lee, J.-S., Lee, H.G., 2016. Improving solubility, stability, and cellular uptake of resveratrol by nanoencapsulation with chitosan and γ-poly (glutamic acid). Colloids Surf., B 147, 224–233.

Kenawy, E., Omer, A., Tamer, T., Elmeligy, M., Eldin, M.M., 2019. Fabrication of biodegradable gelatin/chitosan/cinnamaldehyde crosslinked membranes for antibacterial wound dressing applications. Int. J. Biol. Macromol. 139, 440–448.

Khan, I.M., Ahmad, A., Ullah, M., 2013. Synthesis, spectroscopic investigations, antimicrobial and DNA binding studies of a new charge transfer complex of o-phenylenediamine with 3, 5-dinitrosalicylic acid. Spectrochim. Acta Part A Mol. Biomol. Spectrosc. 102, 82–87.

Kumar, A., Pandith, A., Kim, H.-S., 2016. Pyrenebutylamidopropylimidazole as a multi-analyte sensor for 3, 5-dinitrosalicylic acid and Hg^{2+} ions. J. Lumin. 172, 309–316.

Kumar, S., Nair, R.R., Pillai, P.B., Gupta, S.N., Iyengar, M., Sood, A., 2014. Graphene oxide–$MnFe_2O_4$ magnetic nanohybrids for efficient removal of lead and arsenic from water. ACS Appl. Mater. Interfaces 6, 17426–17436.

Li, F., Jin, H., Xiao, J., Yin, X., Liu, X., Li, D., Huang, Q., 2018a. The simultaneous loading of catechin and quercetin on chitosan-based nanoparticles as effective antioxidant and antibacterial agent. Food Res. Int. 111, 351–360.

Li, Z., Hu, W., Zhao, Y., Ren, L., Yuan, X., 2018b. Integrated antibacterial and antifouling surfaces via cross-linking chitosan-g-eugenol/zwitterionic copolymer on electrospun membranes. Colloids Surf., B 169, 151–159.

Makadia, H.K., Siegel, S.J., 2011. Poly lactic-co-glycolic acid (PLGA) as biodegradable controlled drug delivery carrier. Polymers 3, 1377–1397.

Murali, S., Kumar, S., Koh, J., Seena, S., Singh, P., Ramalho, A., Sobral, A.J., 2019. Bio-based chitosan/gelatin/Ag@ ZnO bionanocomposites: synthesis and mechanical and antibacterial properties. Cellulose, 1–15.

Omidi, S., Kakanejadifard, A., 2019. Modification of chitosan and chitosan nanoparticle by long chain pyridinium compounds: Synthesis, characterization, antibacterial, and antioxidant activities. Carbohydr. Polym. 208, 477–485.

Pawar, V., Bulbake, U., Khan, W., Srivastava, R., 2019. Chitosan sponges as a sustained release carrier system for the prophylaxis of orthopedic implant-associated infections. Int. J. Biol. Macromol. 134, 100–112.

Pinheiro, A.C., Bourbon, A.I., Cerqueira, M.A., Maricato, É., Nunes, C., Coimbra, M.A., Vicente, A.A., 2015. Chitosan/fucoidan multilayer nanocapsules as a vehicle for controlled release of bioactive compounds. Carbohydr. Polym. 115, 1–9.

Pretsch, E., Clerc, T., Seibl, J., Simon, W., 2013. Tables of Spectral Data for Structure Determination of Organic Compounds. Springer Science & Business Media.

Prokhorov, E., España-Sánchez, B., Luna-Bárcenas, G., Padilla-Vaca, F., Cruz-Soto, M., Vázquez-Lepe, M., Kovalenko, Y., Elizalde-Peña, E., 2019. Chitosan/copper nanocomposites: Correlation between electrical and antibacterial properties. Colloids Surf., B 180, 186–192.

Qi, L., Xu, Z., Jiang, X., Hu, C., Zou, X., 2004. Preparation and antibacterial activity of chitosan nanoparticles. Carbohydr. Res. 339, 2693–2700.

Riswan Ahamed, M.A., Azarudeen, R.S., Prabu, N., Burkanudeen, A.R., 2015. Studies of retention and reusable capacities of melamine formaldehyde based terpolymer against some toxic metal ions by batch equilibrium method. Sep. Sci. Technol. 50, 1925–1939.

Sadeghi-Kiakhani, M., Safapour, S., Ghanbari-Adivi, F., 2019. Grafting of chitosan-acrylamide hybrid on the wool: Characterization, reactive dyeing, antioxidant and antibacterial studies. Int. J. Biol. Macromol. 134, 1170–1178.

Salama, A., Diab, M.A., Abou-Zeid, R.E., Aljohani, H.A., Shoueir, K.R., 2018. Crosslinked alginate/silica/zinc oxide nanocomposite: a sustainable material with antibacterial properties. Compos. Commun. 7, 7–11.

Salva, R., Le Meins, J.-F., Sandre, O., Brûlet, A., Schmutz, M., Guenoun, P., Lecommandoux, S., 2013. Polymersome shape transformation at the nanoscale. ACS Nano 7, 9298–9311.

Santos, A.C., Veiga, F., Ribeiro, A.J., 2011. New delivery systems to improve the bioavailability of resveratrol. Expert Opinion on Drug Delivery 8, 973–990.

Sebastian, S., Sylvestre, S., Jayabharathi, J., Ayyapan, S., Amalanathan, M., Oudayakumar, K., Herman, I.A., 2015. Study on conformational stability, molecular structure, vibrational spectra, NBO, TD-DFT, HOMO and LUMO analysis of 3, 5-dinitrosalicylic acid by DFT techniques. Spectrochim. Acta Part A Mol. Biomol. Spectrosc. 136, 1107–1118.

Shaban, N.Z., Yehia, S.A., Shoueir, K.R., Saleh, S.R., Awad, D., Shaban, S.Y., 2019. Design, DNA binding and kinetic studies, antibacterial and cytotoxic activities of stable dithiophenolato titanium (IV)-chitosan nanocomposite. J. Mol. Liq. 287, 111002.

Shinabarger, D., 1999. Mechanism of action of the oxazolidinone antibacterial agents. Expert Opin. Invest. Drugs 8, 1195–1202.

Shoueir R., K., 2020. Green microwave synthesis of functionalized chitosan with robust adsorption capacities for Cr(VI) and/or RHB in complex aqueous solutions. Environ. Sci. Poll. Res. https://doi.org/10.1007/s11356-020-09341-8. In press.

Shoueir, K., Ahmed, M., Gaber, S.A.A., El-Kemary, M., 2020. Thallium and selenite doped carbonated hydroxyapatite: microstructural features and anticancer activity assessment against human lung carcinoma. Ceram. Int. 46, 5201–5212.

Shoueir, K., El-Sheshtawy, H., Misbah, M., El-Hosainy, H., El-Mehasseb, I., El-Kemary, M., 2018. Fenton-like nanocatalyst for photodegradation of methylene blue under visible light activated by hybrid green DNSA@ Chitosan@ $MnFe_2O_4$. Carbohydr. Polym. 197, 17–28.

Shoueir, K.R., Atta, A.M., Sarhan, A.A., Akl, M.A., 2017. Synthesis of monodisperse core shell PVA@ P (AMPS-co-NIPAm) nanogels structured for pre-concentration of Fe (III) ions. Environ. Technol. 38, 967–978.

Song, J., Feng, H., Wu, M., Chen, L., Xia, W., Zhang, W., 2020. Preparation and characterization of arginine-modified chitosan/hydroxypropyl methylcellulose antibacterial film. Int. J. Biol. Macromol. 145, 750–758.

Stein, G.E., Wells, E.M., 2010. The importance of tissue penetration in achieving successful antimicrobial treatment of nosocomial pneumonia and complicated skin and soft-tissue infections caused by methicillin-resistant Staphylococcus aureus: vancomycin and linezolid. Curr. Med. Res. Opin. 26, 571–588.

Tammaro, L., Saturnino, C., D'Aniello, S., Vigliotta, G., Vittoria, V., 2015. Polymorphic solidification of Linezolid confined in electrospun PCL fibers for controlled release in topical applications. Int. J. Pharm. 490, 32–38.

Wang, J., Jiang, J.-Z., Chen, W., Bai, Z.-W., 2016. Data of $^1H/^{13}C$ NMR spectra and degree of substitution for chitosan alkyl urea. Data in brief 7, 1228–1236.

Wang, Q., Jiang, H., Li, Y., Chen, W., Li, H., Peng, K., Zhang, Z., Sun, X., 2017. Targeting NF-kB signaling with polymeric hybrid micelles that co-deliver siRNA and dexamethasone for arthritis therapy. Biomaterials 122, 10–22.

Wang, Y., Zhou, P., Xiao, D., Zhu, Y., Zhang, J., Sui, X., Feng, X., Xu, H., Mao, Z., 2019. Chitosan-bound carboxymethylated cotton fabric and its application as wound dressing. Carbohydr. Polym. 221, 202–208.

Xie, R., Zhang, X.D., Zhao, Q., Peng, B., Zheng, J., 2018. Analysis of global prevalence of antibiotic resistance in Acinetobacter baumannii infections disclosed a faster increase in OECD countries. Emerging Microbes Infect. 7, 1–10.

Yusof, N.A.A., Zain, N.M., Pauzi, N., 2019. Synthesis of ZnO nanoparticles with chitosan as stabilizing agent and their antibacterial properties against Gram-positive and Gram-negative bacteria. Int. J. Biol. Macromol. 124, 1132–1136.